**Supporting Information for**

# Behavior of Citrate-Capped Ultra-Small Gold Nanoparticles on a Supported Lipid Bilayer Interface at Atomic Resolution

*Rashad Kariuki,[1] Rowan Penman,[1] Saffron J. Bryant,[1] Rebecca Orrell-Trigg,[1] Nastaran Meftahi,[2] Russell J. Crawford,[1] Chris F. McConville,[1,3] Gary Bryant,[1] Kislon Voïtchovsky,[4] Charlotte E. Conn,[1] Andrew J. Christofferson,[1,2]* and Aaron Elbourne [1,]**

[1]School of Science, STEM College, RMIT University, Melbourne VIC 3001, Australia.
[2]ARC Centre of Excellence in Exciton Science, School of Science, RMIT University, Melbourne, VIC 3001, Australia.
[3]Deakin University, Geelong, VIC 3220, Australia.
[4]University of Durham, Physics Department, Durham DH1 3LE, UK.

* Corresponding Authors
E-mail: andrew.christofferson@rmit.edu.au
E-mail: aaron.elbourne@rmit.edu.au

## Supporting Information

**Supported Lipid Bilayer Formation:** For all experiments, surface-adsorbed flat lipid bilayers were formed via the previously reported vesicle fusion method (see Figure S1, schematic).[1-3] At low concentrations, supported lipid bilayer patches (SLBPs) are known to spontaneously form at the mica surface (See Figure S1). In contrast, at higher concentrations, the underlying mica surface is completely covered by an almost continuous supported lipid bilayer (SLB) (see Figure S1). Figure S3 show representative low-resolution (5 µm × 5 µm) and high-resolution (500 nm × 500 nm) AFM images of the DOPC and DPPC SLBPs. Height analysis (see height profile, white line, bottom left of the images) reveals the bilayer thicknesses. This value is commensurate with the known thickness of the respective lipid bilayers.
AFM images of the interface at low concentrations (Figure S1.3.) reveal raised, disc-like features of variable sub-500 nm width. These objects are characteristic of SLBP – regions of flat-lipid bilayer which result from suspended small unilamellar vesicles (SUVs) rupturing, and contouring, to the underlying mica surface. SLBs form at this concentration as there is not enough lipidic material to achieve full surface coverage.

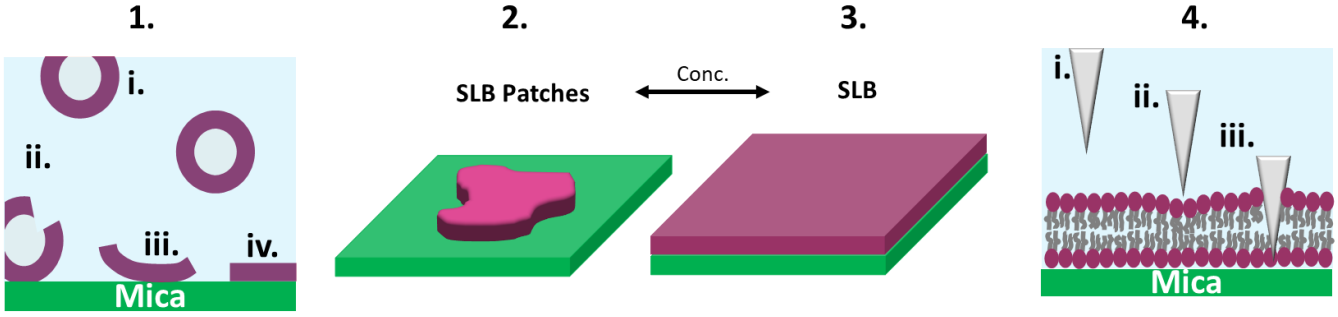


**Figure S1.** Schematic representation of **1.** Vesicle fusion of SLB at the mica interface. Concentration-dependent formation of **2.** SLB patches and **3.** SLBs. **4.** An AFM cantilever (i) moving towards, (ii) coming into contact with, and (iii) rupturing a SLB.

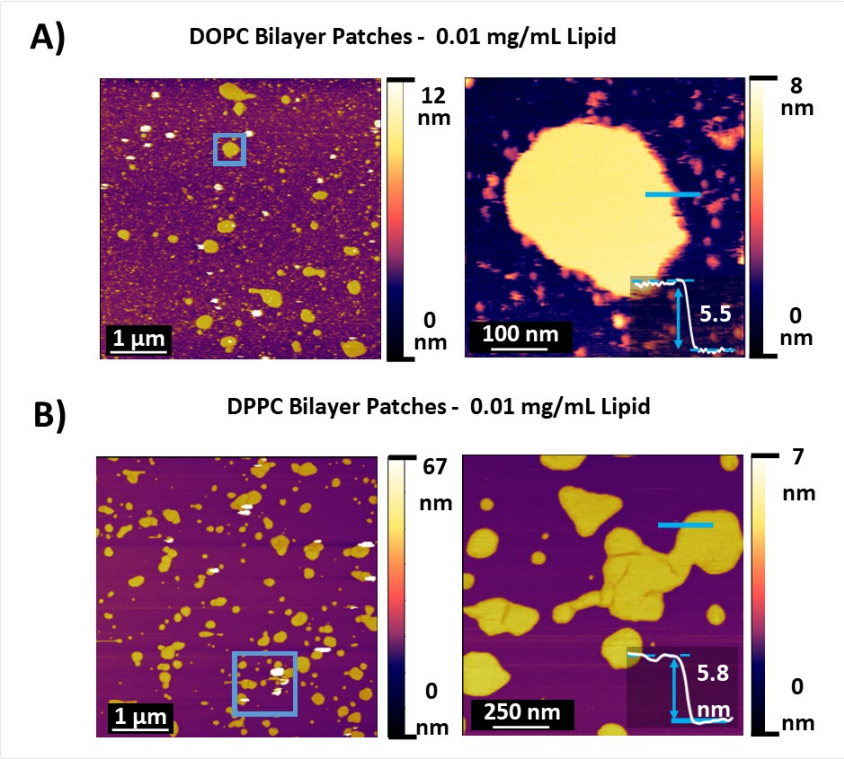


**Figure S2.** AFM height images of lipid bilayer patches at low and high magnification for A) DOPC and B) DPPC.

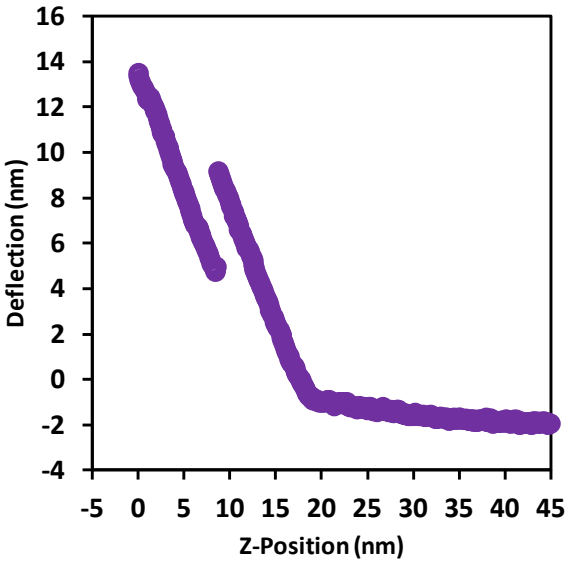


**Figure S3.** Raw AFM Force curve showing the untreated data for a DOPC-mica system. The data is presented as relative Z-position vs. the cantilevers deflection in nm.

**Particle Characterization.** Figure S4 shows characterization data for the AuNPs used in this study, which provides a baseline for analysis. Transmission electron microscopy (TEM) was employed to visualize the commercially obtained, citrated-capped AuNPs. Figure S4A and S4B show lower-magnification images of the spherical, monodispersed AuNPs with roughly uniform diameters. Size analysis of 100 individual AuNPs within multiple TEM images showed an average diameter 5.0 nm ± 0.6 nm (see Figure S4C). This data is shown in the histogram in Figure S4C. A high-magnification HRTEM image of a single AuNP highlights the atomic lattice of the particles, with a distinct lattice dimension of 0.23 nm (see Figure S4D). This lattice spacing is consistent with face-centered cubic (FCC) AuNPs imaged along the (111) planes, suggesting that the material is elemental gold.[4] This result is unsurprising as FCC gold is typical of standard AuNPs and the material itself is largely inert. Together, this data provides a baseline for assessment of the nanoparticle-SLB interface following AuNP introduction (discussed below). Dynamic light scattering (DLS) (see Figure S4E) revealed a bimodal average size distribution, with a peak at ~5 nm (red arrow) and ~69 nm (blue arrow). The emergence of two sizes within the AuNP population is not unsurprising as nanoparticle systems often aggregate in solution.[5, 6] This data is commensurate with the TEM obtained, which reveal a mixture of single particles and particle aggregates (or particle clusters) (see Figure S4A and S4B). A model bare AuNP is shown in Figure S4F.

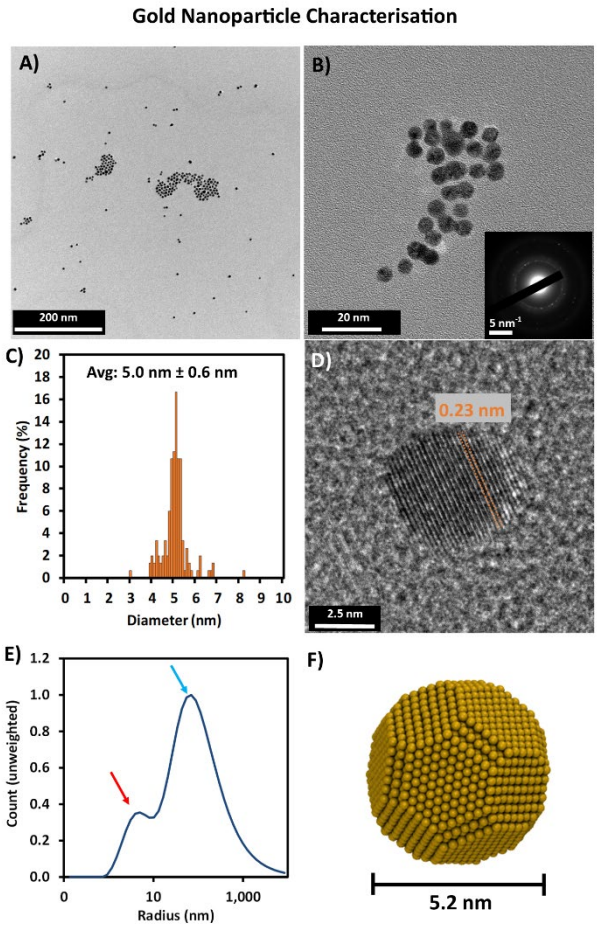


**Figure S4. Nanoparticle Characterization. A)** Low-resolution TEM image of the AuNPs. **B)** Histogram of the measured AuNP diameters as measured by analysis of multiple TEM images of AuNPs (n = 100 particles). The average diameter of the particles was measured at 5.0 nm ± 0.6 nm. **C)** Higher resolution image of the AuNPs. The selected area electron diffraction (SAED) image is shown as an inset to bottom right. **D)** Atomic resolution TEM image of a single gold nanoparticle. The atomic lattice of the material can be observed with an inter-atom spacing of 0.23 nm. This lattice spacing is consistent with the (111) planes of face-centered cubic (FCC) AuNPs.[4] **E)** DLS AuNP radial size distribution **F)** Image of a bare AuNP from MD simulations.

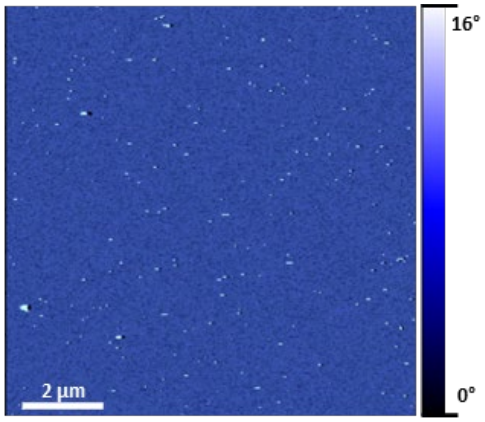


**Figure S5.** Phase images of a DOPC SLBs obtained following introduction of the AuNPs.

## Imaging Force Calculation:

The maximum average imaging force ($F_{avg}$) used during the AM-AFM experiments can be approximated using the following equations;[7]

$$F_{avg} = k_c A_0 \frac{4\pi^2}{3}\left(\frac{\tau}{T}\right)^2 \quad (1)$$

and

$$\frac{\tau}{T} = \frac{arccos\left[\frac{(A_0 - \Delta A)}{A_0}\right]}{2\pi} \quad (2)$$

where, $A_0$ is the free liquid amplitude (~ 6 nm), $\Delta A$ is the change in amplitude upon surface engagement, also referred to as the damped oscillation (~3 – 4 nm), and $K_c$ is the cantilever spring constant. Under these conditions, the max $F_{avg}$ was consistently maintained between ~0.1 nN and 0.2 nN (see Figure S3. This value is significantly below the required force to rupture the lipid bilayer (See Figure 4B and 4C).

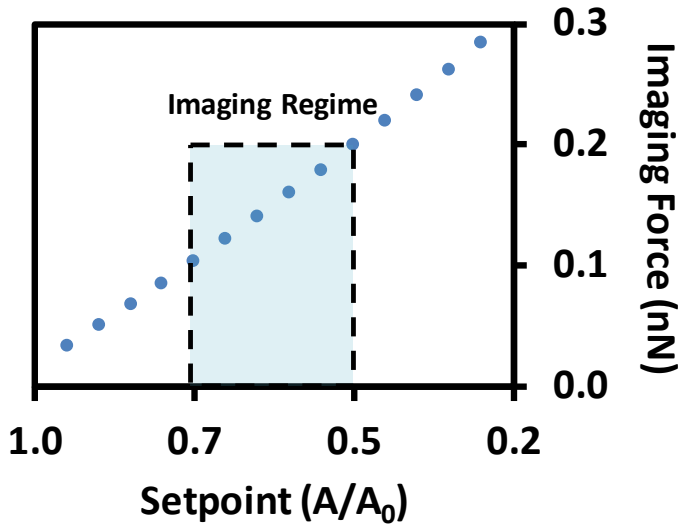


**Figure S6.** Calculated imaging force as a function of $A/A_0$. The $A/A_0$ range used in the experiments here is marked on the graph.

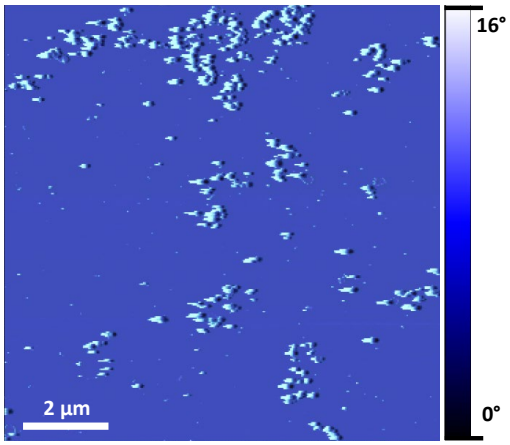


**Figure S7.** Phase images of a DPPC SLBs obtained following introduction of the AuNPs.

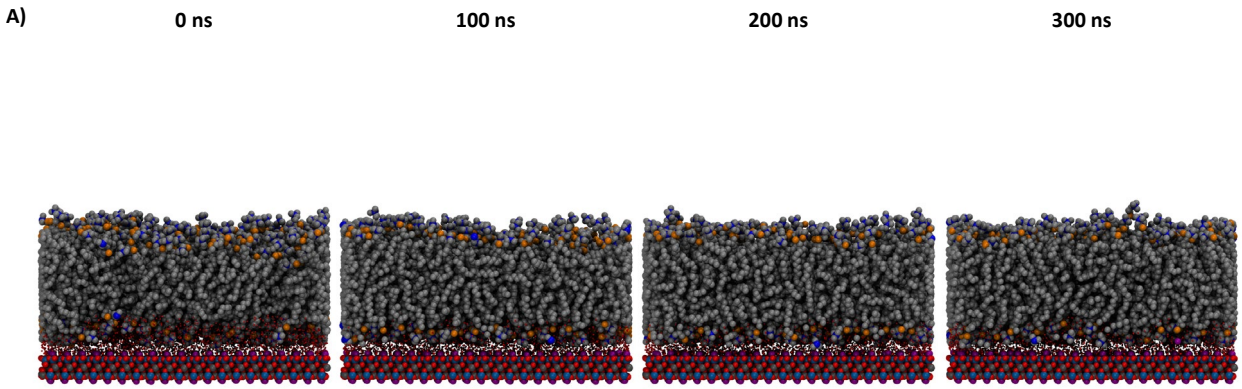


**Figure S8.** MD simulation snapshots of DOPC-SLB.

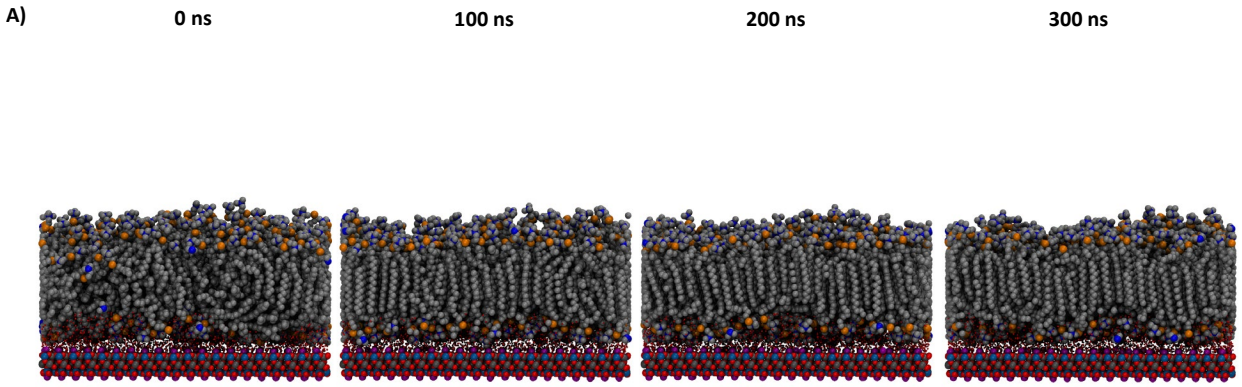


**Figure S9.** MD simulation snapshots of DPPC-SLB.

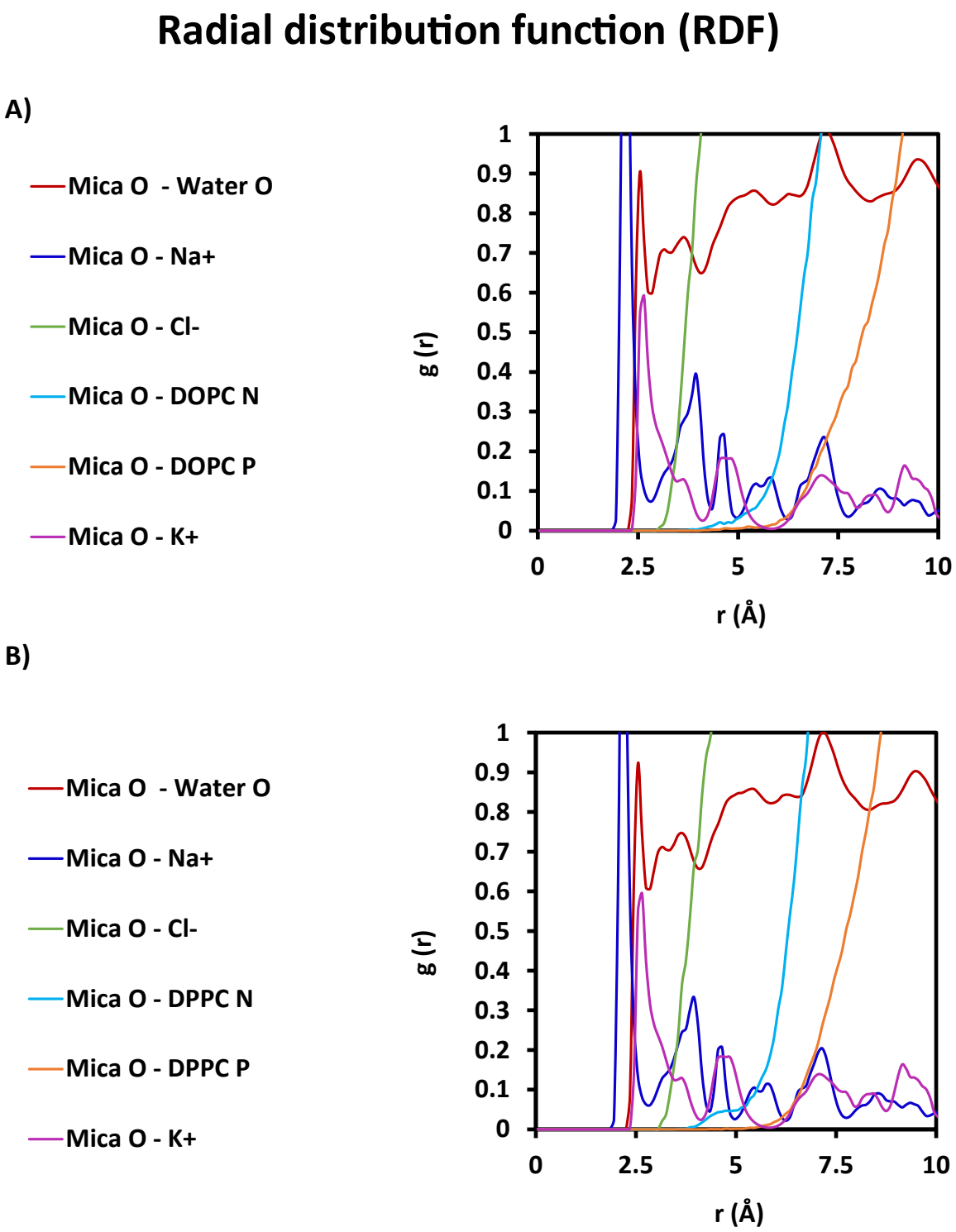


**Figure S10. Pairwise radial distribution function (RDF) between mica oxygen and interfacial species for A)** DOPC and **B)** DPPC. All RDFs were calculated over the final 10 ns of the 300 ns trajectory.

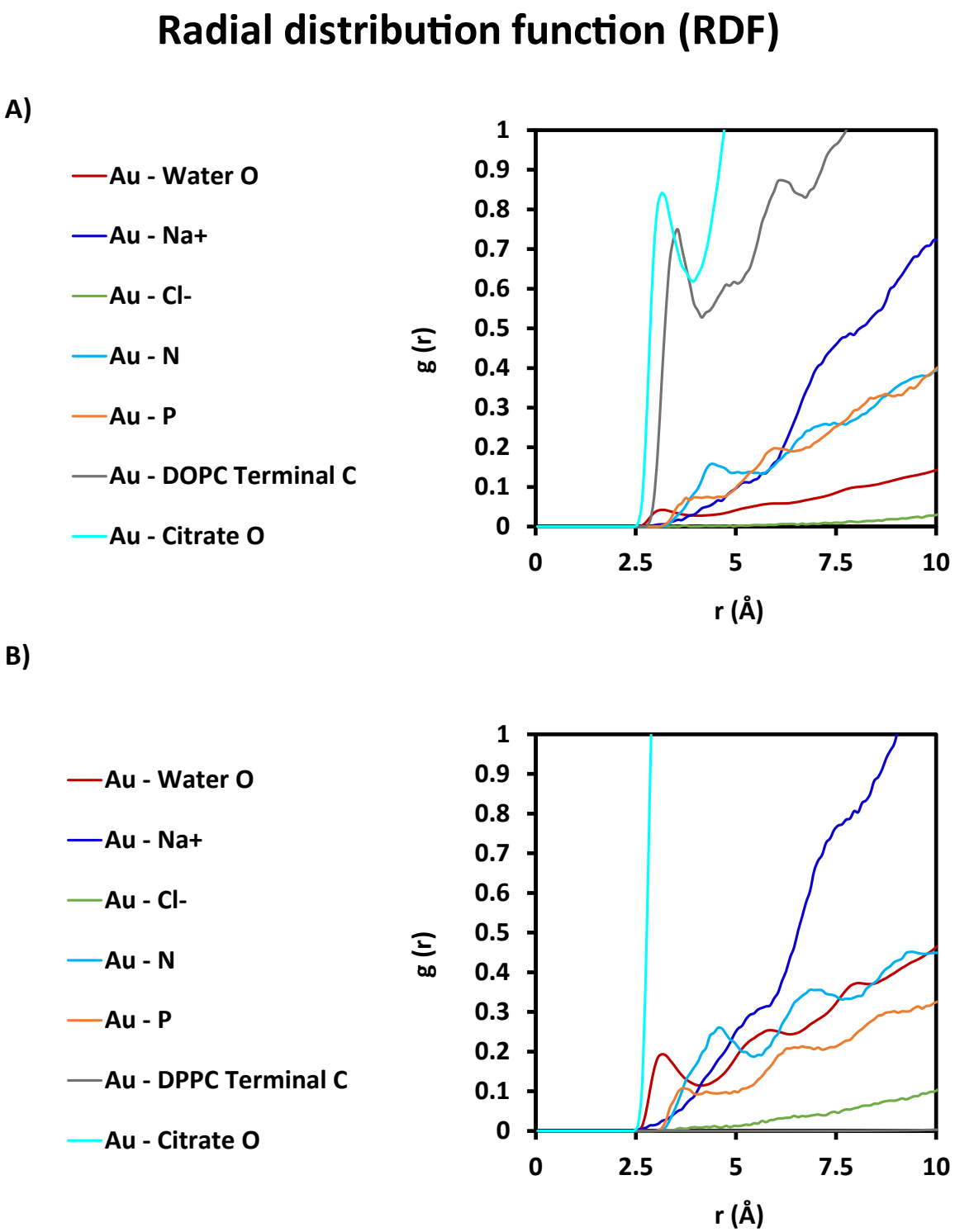


**Figure S11. Pairwise radial distribution function (RDF) between Au and other species for A)** DOPC and **B)** DPPC. All RDFs were calculated over the final 10 ns of the 300 ns trajectory.

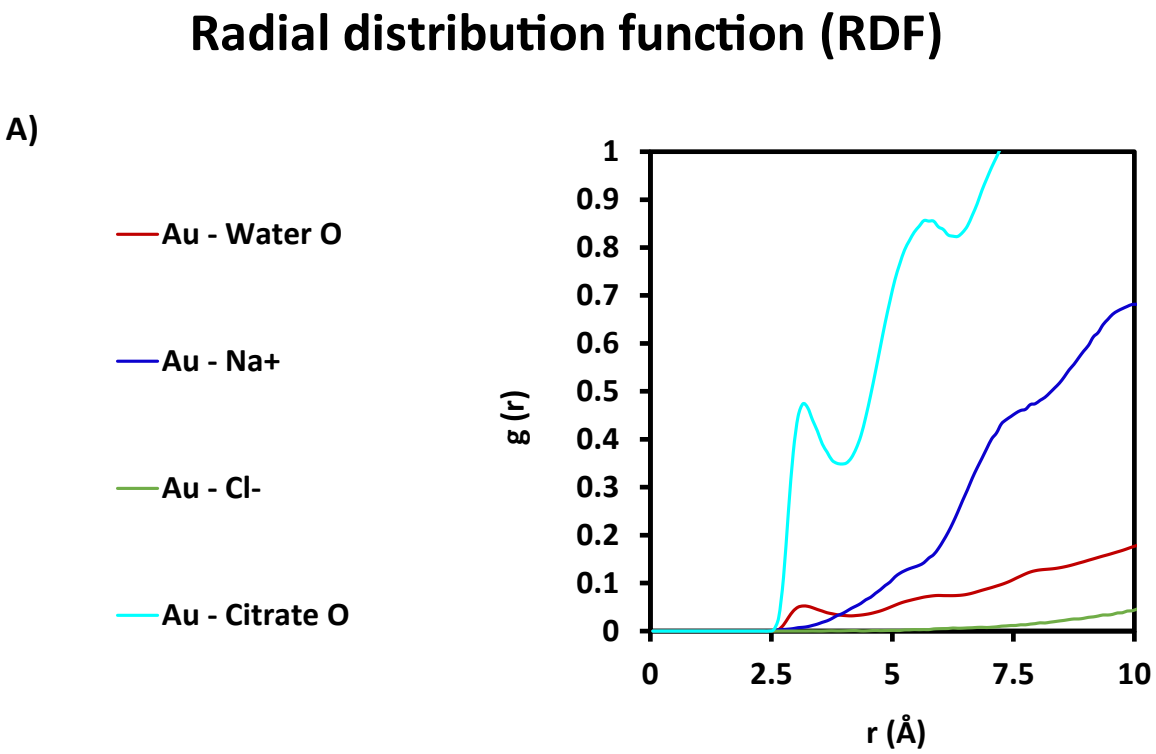


**Figure S12. Pairwise radial distribution function (RDF) between Au and other species for A)** Au. All RDFs were calculated over the final 10 ns of the 300 ns trajectory.

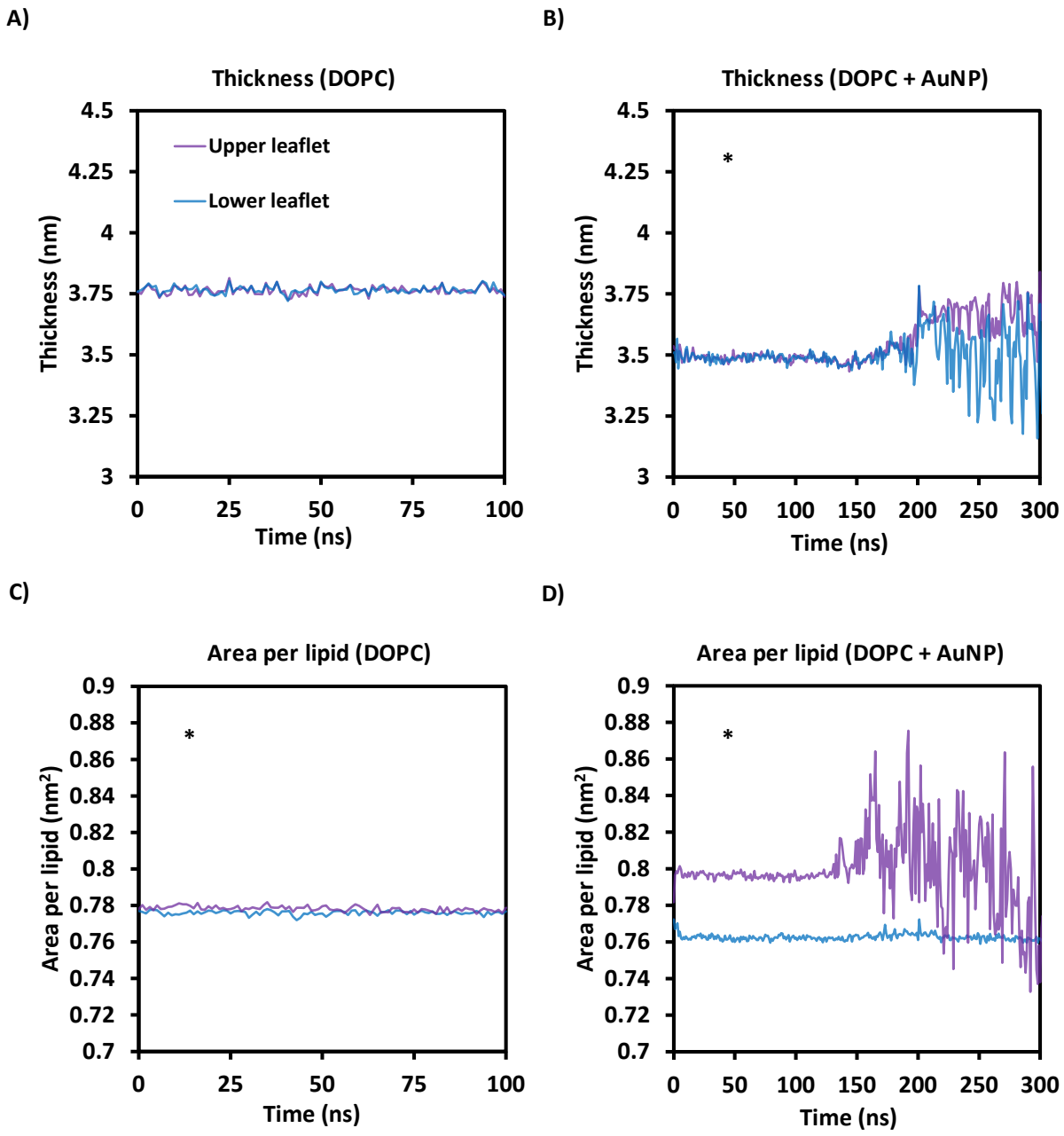


**Figure S13. Membrane thickness and area per lipid (APL) calculations for DOPC as a function of P-headgroup location *via* FATSLiM. A)** Membrane thickness of DOPC-SLB. **B)** Membrane thickness of DOPC_SLB during AuNP interaction. **C)** APL of DOPC-SLB. **D)** APL of DOPC-SLB during AuNP interaction. (*Indicates identical legend.)

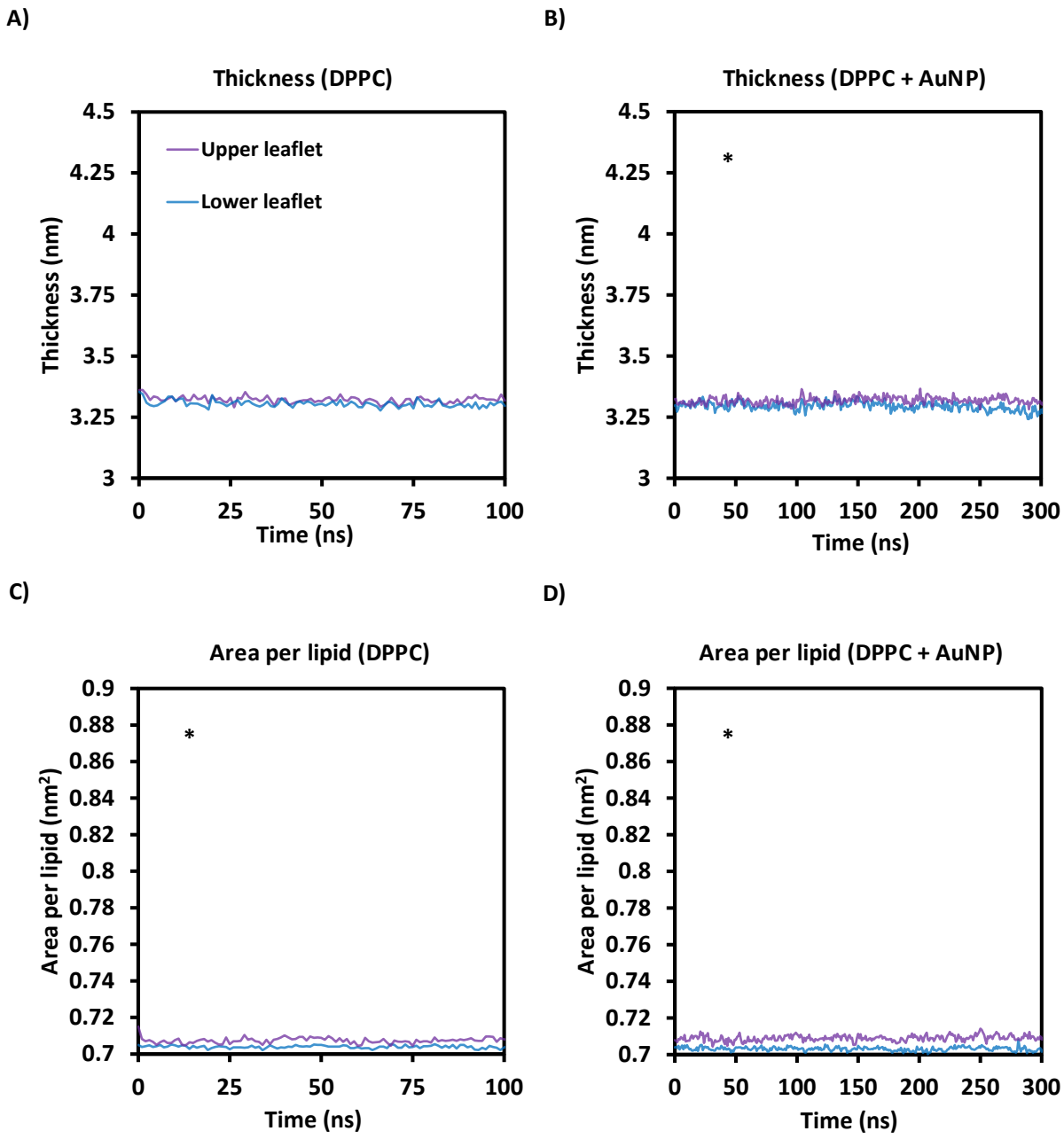


**Figure S14. Membrane thickness and APL calculations for DPPC as a function of P-headgroup location *via* FATSLiM. A)** Membrane thickness of DPPC-SLB. **B)** Membrane thickness of DPPC_SLB during AuNP interaction. **C)** APL of DPPC-SLB. **D)** APL of DPPC-SLB during AuNP interaction. (*Indicates identical legend.)

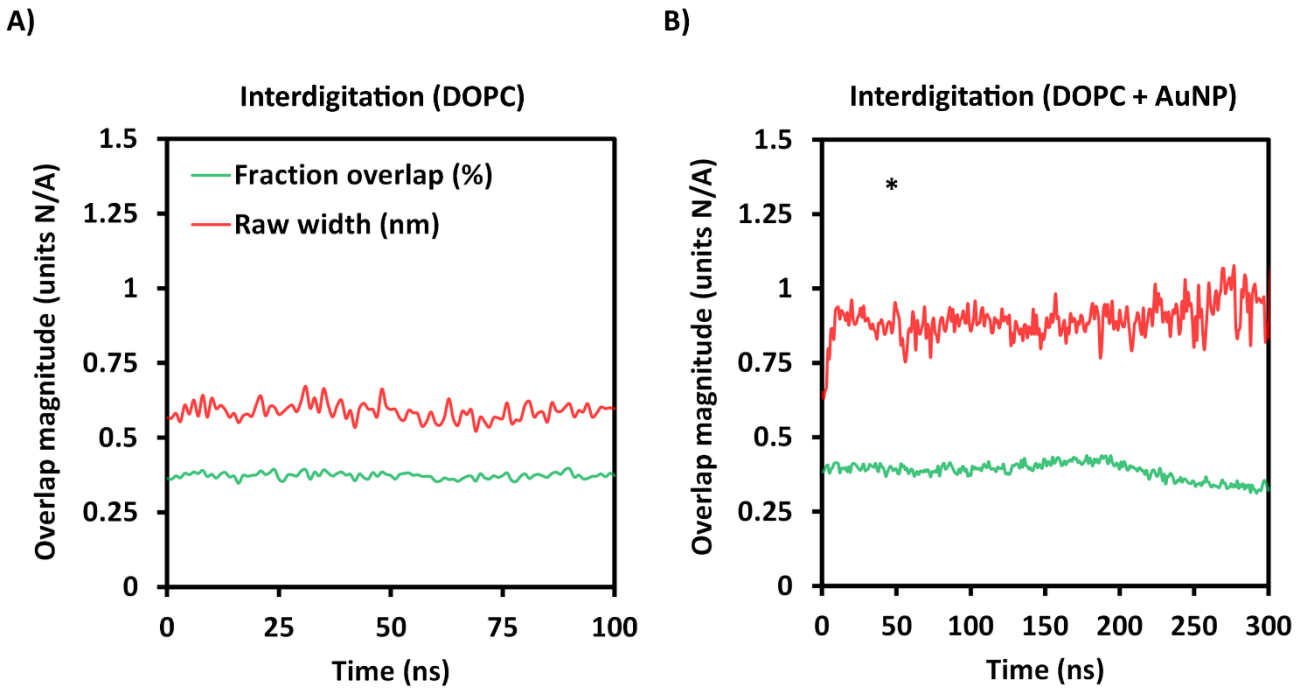


**Figure S15. Interleaflet interdigitation of DOPC as a function of carbon chain coupling. A)** Interdigitation of DOPC-SLB. **B)** Interdigitation of DOPC-SLB during AuNP interaction. (*Indicates identical legend.)

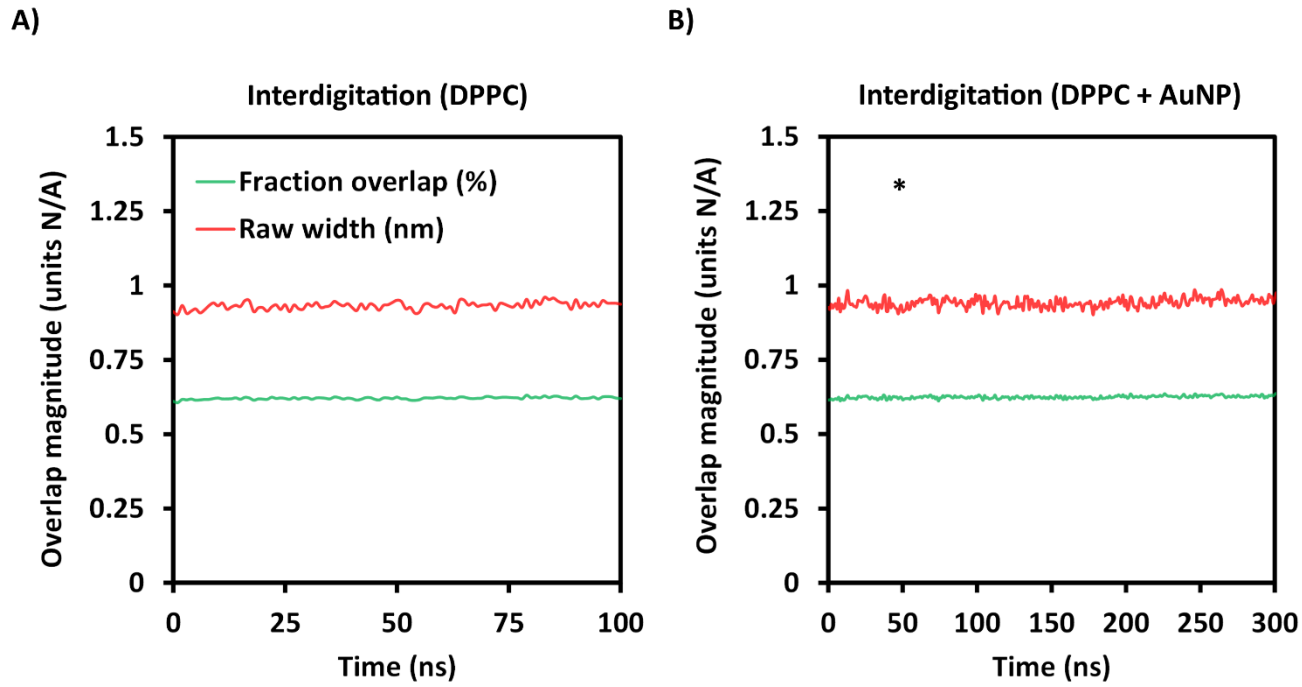


**Figure S16. Interleaflet interdigitation of DPPC as a function of carbon chain coupling. A)** Interdigitation of DOPC-SLB. **B)** Interdigitation of DOPC-SLB during AuNP interaction. (*Indicates identical legend.)

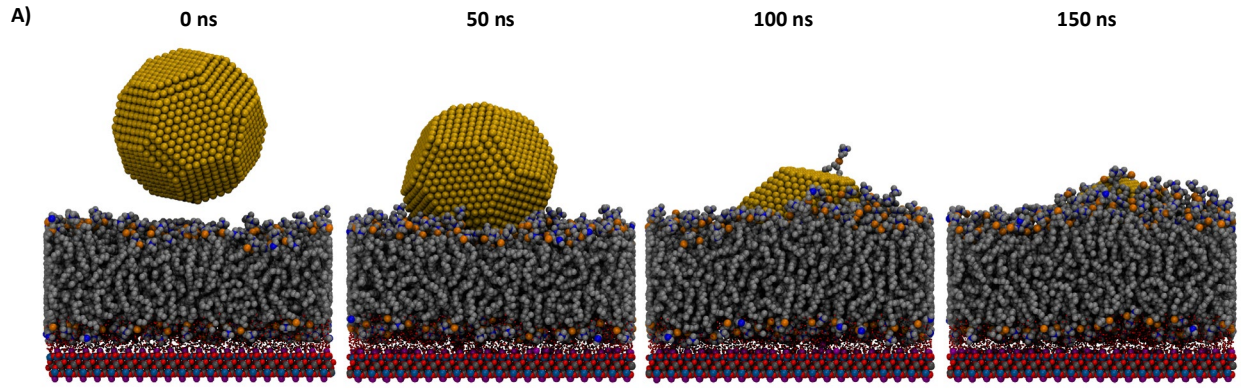


**Figure S17.** MD simulation snapshots of DOPC-SLB with bare (no citrate cap) AuNP.

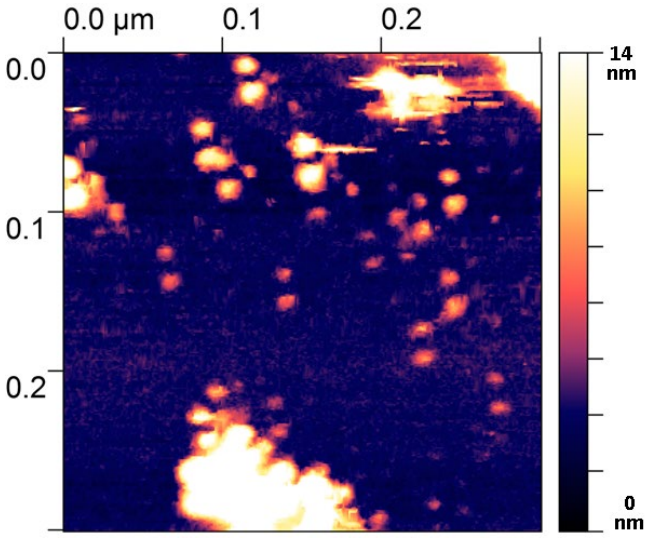


**Figure S18. Low-resolution image of the DOPC-AuNP interface.** Regions of AuNP clustering can be clearly seen.

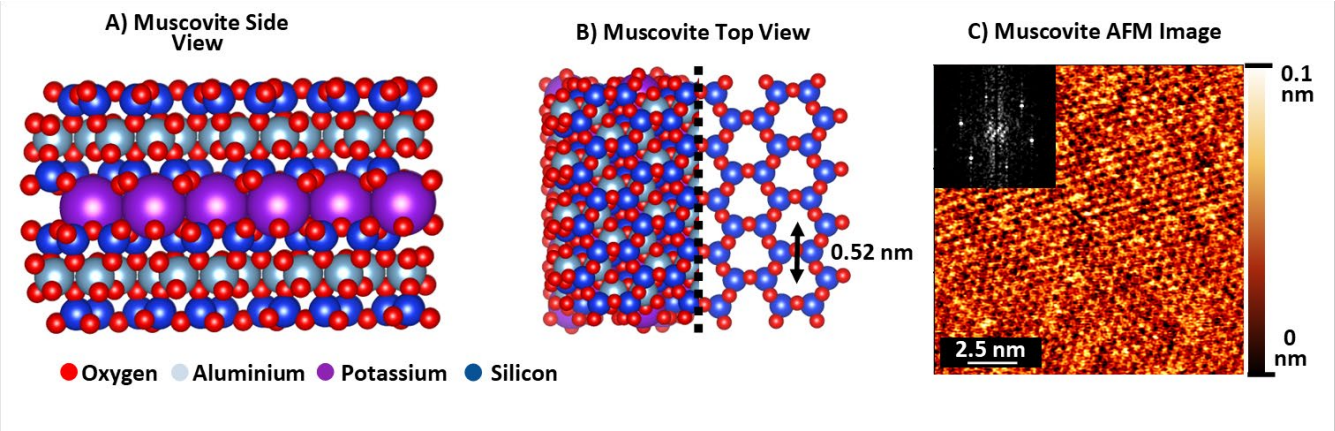


**Figure S19. A)** Side view and **B)** Top-down, basal plane view of the crystal structure of muscovite (mica). Atom colour code is shown below the images. **C)** Atomic-resolution AFM images of the mica surface obtained in 150 mM NaCl. The periodic, hexag-onal structure of the atomic lattice can be clearly seen with a repeat spacing of 0.52 nm. This highlights the resolution of the AFM used to obtain the work shown here.

## Supporting methods

**Adjustment of Lennard-Jones interactions between Au and other atoms.** The use of unmodified Lennard-Jones parameters for the pairwise interactions between Au atoms and all other atoms resulted in a citrate cap of ~215 citrate molecules that were not displaced upon contact with the DOPC membrane (Figure S19).

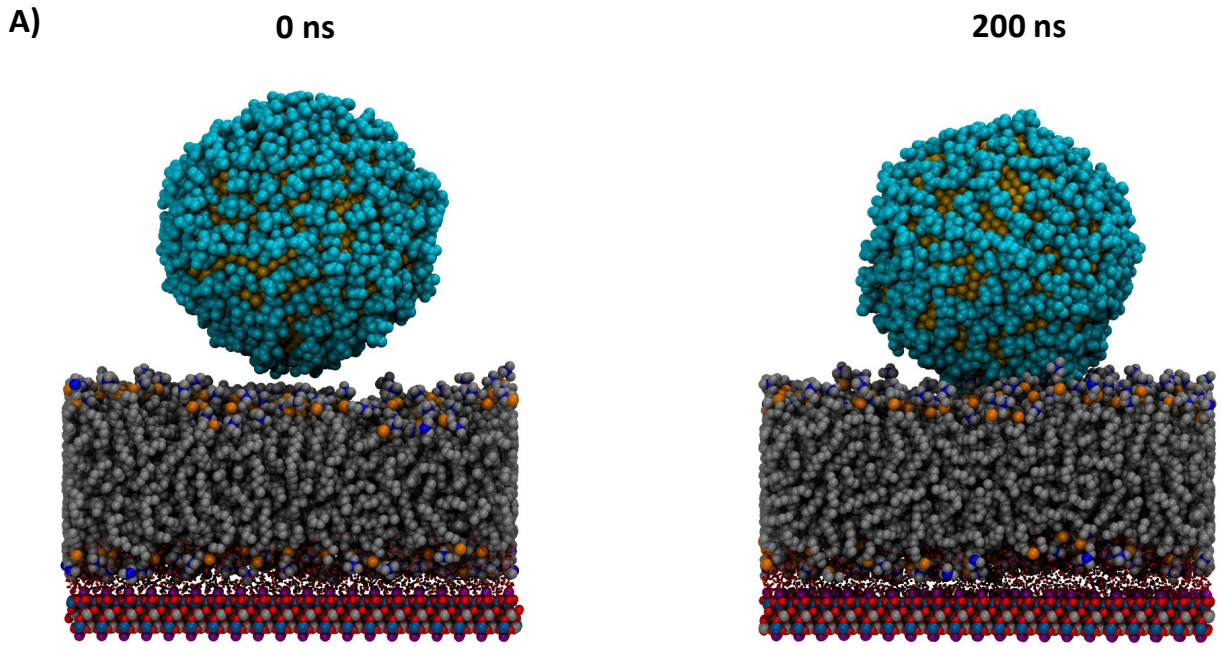


**Figure S20.** Simulation of citrate-capped AuNP on DOPC-SLB using unmodified parameters. A) AuNP surrounded by 212 citrate ions at 0 ns of MD simulation. B) AuNP after 150 ns of simulation (only citrate within 5 Å of Au shown).

Multiple citrate coverages were tested, including removing the citrate between the AuNP and the membrane, but the AuNP failed to penetrate the DOPC membrane with any citrate coverage using the default Au parameters. We therefore modified the interaction between Au atoms and all other atoms by adjusting the Au epsilon value ($\varepsilon_{Au}$) and calculating the pairwise interactions using the geometric combination rule: $\varepsilon_{Auj} = (\varepsilon_{Au} \times \varepsilon_j)^{1/2}$, where $\varepsilon_j$ is the epsilon value for every other atom type in the system. The modified $\varepsilon_{Au}$ value of was considered acceptable when it provided a reasonable citrate surface coverage (~150 citrate within 0.5 nm of Au) that was displaced upon contact with the DOPC membrane. The $\varepsilon_{Au}$ value determined in this work was 3.5. The final non-bond parameters, formatted for the GROMACS MD code, are shown in Table S1.

**Table S1.** Modified non-bond parameters for pairwise interaction between Au atoms and all other atom types, formatted for the [ nonbond_params ] section of the GROMACS forcefield.itp file.

| i | j | func | sigma | epsilon |
|---|---|---|---|---|
| AU | HAL1 | 1 | 2.49050737E-01 | 5.67598450E-01 |
| AU | HAL2 | 1 | 2.50832534E-01 | 6.40337411E-01 |
| AU | HAL3 | 1 | 2.50832534E-01 | 5.92837246E-01 |
| AU | HEL1 | 1 | 2.42814446E-01 | 6.73768506E-01 |
| AU | HL | 1 | 1.93815016E-01 | 8.20746002E-01 |
| AU | HT | 1 | 1.51452782E-01 | 8.20746002E-01 |
| AU | CEL1 | 1 | 3.17649938E-01 | 9.97893782E-01 |
| AU | CL | 1 | 3.09631849E-01 | 1.01246234E+00 |
| AU | CTL1 | 1 | 3.34131564E-01 | 5.41183887E-01 |
| AU | CTL2 | 1 | 3.10522748E-01 | 9.05573851E-01 |
| AU | CTL3 | 1 | 3.13195444E-01 | 1.06875254E+00 |
| AU | CTL5 | 1 | 3.14977242E-01 | 1.08236777E+00 |
| AU | NTL | 1 | 2.96268369E-01 | 1.71137372E+00 |
| AU | O2L | 1 | 2.82904888E-01 | 1.32562438E+00 |
| AU | OBL | 1 | 2.82904888E-01 | 1.32562438E+00 |
| AU | OSL | 1 | 2.78450394E-01 | 1.21012396E+00 |
| AU | OSLP | 1 | 2.78450394E-01 | 1.21012396E+00 |
| AU | OT | 1 | 2.88980817E-01 | 1.49243171E+00 |
| AU | SOD | 1 | 2.57135643E-01 | 8.28736146E-01 |
| AU | PL | 1 | 3.22995330E-01 | 2.92689938E+00 |
| AU | CLA | 1 | 3.33686115E-01 | 1.48209311E+00 |
| AU | CG321 | 1 | 3.10522748E-01 | 9.05573851E-01 |
| AU | CG2O2 | 1 | 2.82904888E-01 | 1.19796160E+00 |
| AU | OG2D1 | 1 | 2.82904888E-01 | 1.32562438E+00 |
| AU | CG301 | 1 | 3.09631849E-01 | 6.84549487E-01 |
| AU | OG311 | 1 | 2.88695730E-01 | 1.67723356E+00 |
| AU | HGA2 | 1 | 2.50832534E-01 | 7.15918990E-01 |
| AU | CG2O3 | 1 | 3.09631849E-01 | 1.01246234E+00 |
| AU | HGP1 | 1 | 1.51452782E-01 | 8.20746002E-01 |
| AU | OG2D2 | 1 | 2.82904888E-01 | 1.32562438E+00 |
| AU | IHOY | 1 | 1.79783361E-01 | 8.20746002E-01 |
| AU | IOY1 | 1 | 2.87359382E-01 | 4.68678995E-01 |
| AU | IOY2 | 1 | 2.87359382E-01 | 6.05061980E-01 |
| AU | IOY3 | 1 | 2.87359382E-01 | 6.05061980E-01 |
| AU | IOY4 | 1 | 2.87359382E-01 | 6.05061980E-01 |
| AU | IOY5 | 1 | 2.87359382E-01 | 6.05061980E-01 |
| AU | IOY6 | 1 | 2.87359382E-01 | 6.05061980E-01 |
| AU | IOY7 | 1 | 2.87359382E-01 | 6.05061980E-01 |
| AU | IOY8 | 1 | 2.87359382E-01 | 6.05061980E-01 |
| AU | IOY9 | 1 | 2.87359382E-01 | 6.05061980E-01 |
| AU | IAY1 | 1 | 3.18540837E-01 | 8.55686859E-01 |
| AU | IAY2 | 1 | 3.18540837E-01 | 8.55686859E-01 |
| AU | IAYT2 | 1 | 3.18540837E-01 | 8.55686859E-01 |
| AU | ISY1 | 1 | 3.09631849E-01 | 8.55686859E-01 |
| AU | ISY2 | 1 | 3.09631849E-01 | 8.55686859E-01 |
| AU | IK_CM | 1 | 3.00722862E-01 | 1.71137372E+00 |

**Supporting References**

(1) Lv, Z.; Banerjee, S.; Zagorski, K.; Lyubchenko, Y. L. Supported Lipid Bilayers for Atomic Force Microscopy Studies. *Methods Mol Biol* **2018**, *1814*, 129-143. DOI: 10.1007/978-1-4939-8591-3_8 PubMed.
(2) Seeger, H. M.; Cerbo, A. D.; Alessandrini, A.; Facci, P. Supported lipid bilayers on mica and silicon oxide: comparison of the main phase transition behavior. *The Journal of Physical Chemistry B* **2010**, *114* (27), 8926-8933.
(3) Seantier, B.; Breffa, C.; Félix, O.; Decher, G. In Situ Investigations of the Formation of Mixed Supported Lipid Bilayers Close to the Phase Transition Temperature. *Nano Letters* **2004**, *4* (1), 5-10. DOI: 10.1021/nl034590l.
(4) Gao, Z.; Su, R.; Huang, R.; Qi, W.; He, Z. Glucomannan-mediated facile synthesis of gold nanoparticles for catalytic reduction of 4-nitrophenol. *Nanoscale research letters* **2014**, *9* (1), 404.
(5) Albanese, A.; Chan, W. C. W. Effect of Gold Nanoparticle Aggregation on Cell Uptake and Toxicity. *ACS Nano* **2011**, *5* (7), 5478-5489. DOI: 10.1021/nn2007496.
(6) Chegel, V.; Rachkov, O.; Lopatynskyi, A.; Ishihara, S.; Yanchuk, I.; Nemoto, Y.; Hill, J. P.; Ariga, K. Gold Nanoparticles Aggregation: Drastic Effect of Cooperative Functionalities in a Single Molecular Conjugate. *The Journal of Physical Chemistry C* **2012**, *116* (4), 2683-2690. DOI: 10.1021/jp209251y.
(7) Putman, C. A. J.; Werf, K. O. V. d.; Grooth, B. G. D.; Hulst, N. F. V.; Greve, J. Tapping mode atomic force microscopy in liquid. *Applied Physics Letters* **1994**, *64* (18), 2454-2456. DOI: 10.1063/1.111597.